AIAA 2000-4221

COMPUTATION OF VISCOUS FLOW FOR A BOEING 777 AIRCRAFT IN LANDING CONFIGURATION

Stuart E. Rogers and **Karlin Roth**
NASA Ames Research Center
Moffett Field, California

Hoa V. Cao
The Boeing Company
Seattle, Washington

Jeffrey P. Slotnick and **Mark Whitlock**
The Boeing Company
Long Beach, California

Steven M. Nash and **M. David Baker**
MCAT, Inc.; NASA Ames Research Center
Moffett Field, California

18th AIAA Applied Aerodynamics Conference

14 - 17 August 2000 / Denver, Colorado

For permission to copy or republish, contact the American Institute of Aeronautics and Astronautics
1801 Alexander Bell Drive, Suite 500, Reston, VA 20191–4344

AIAA 2000-4221

COMPUTATION OF VISCOUS FLOW FOR A BOEING 777 AIRCRAFT IN LANDING CONFIGURATION

Stuart E. Rogers* and **Karlin Roth**†
NASA Ames Research Center
Moffett Field, California

Hoa V. Cao ‡
The Boeing Company
Seattle, Washington

Jeffrey P. Slotnick§ and **Mark Whitlock** ¶
The Boeing Company
Long Beach, California

Steven M. Nash‖ and **M. David Baker** ‖
MCAT, Inc.; NASA Ames Research Center
Moffett Field, California

Abstract

A series of Navier-Stokes simulations of a complete Boeing 777-200 aircraft configured for landing is obtained using a structured overset grid process and the OVERFLOW CFD code. At approach conditions, the computed forces for the 777 computation are within 1.5% of experimental data for lift, and within 4% for drag. The computed lift is lower than the experiment at maximum-lift conditions, but shows closer agreement at post-stall conditions. The effect of sealing a spanwise gap between leading edge elements, and adding a chine onto the nacelle is computed at a high angle of attack. These additions make a significant difference in the flow over the wing near these elements. Detailed comparisons between computed and experimental surface pressures are shown. Good agreement is demonstrated at lower angles of attack, including a prediction of separated flow on the outboard flap.

Introduction

Calculating the viscous fluid flow over a high-lift system of a subsonic commercial aircraft is one of the most difficult problems in Computational Fluid Dynamics (CFD). Even in two-dimensions (2D), state-of-the-art CFD codes fail to consistently predict, with sufficient accuracy, trends with Reynolds number or trends with flap/slat rigging changes.[1] High-lift flow-field analysis is also a very important problem for commercial aircraft companies; the payoffs for understanding it and designing a more efficient high-lift system for commercial jet transports are quite high.[2] Increases in lift coefficient (CL) and in lift-over-drag can lead to a simpler high-lift system, resulting in less weight and less noise, as well as increases in both payload and range.

The difficulties in simulating high-lift flows come from the severe complexity of both the geometry and the flow field. The complexity of the flow field stems from the wing having multi-elements with very small gaps between them, leading to an interaction of various viscous flow phenomena. As stated by Meredith,[2] these flow phenomena include boundary-layer transition, shock and boundary-layer interactions, viscous-wake interactions, confluent wakes and boundary layers, and separated flows. Since the fluid dynamics is dominated by viscous effects, only a high-fidelity simulation using the Navier-Stokes equations can provide the accuracy necessary to assist in aircraft design.

Under the Integrated Wing Design (IWD) element of the NASA Advanced Subsonic Technology (AST) Program, a significant effort was focused on developing the CFD software tools required to perform pro-

*Aerospace Engineer.
†Chief, Aerospace Operations Modeling Office. Senior Member AIAA.
‡Principal Engineer.
§Principal Engineer. Senior Member AIAA.
¶Engineer/Scientist Specialist. Member AIAA.
‖Research Engineer.

Copyright © 2000 by the American Institute of Aeronautics and Astronautics, Inc. No copyright is asserted in the United States under Title 17, U.S. Code. The U.S. Government has a royalty-free license to exercise all rights under the copyright claimed herein for Governmental Purposes. All other rights are reserved by the copyright owner.

duction level CFD analysis of three-dimensional (3D) high-lift systems on complete transport configurations. One of the program milestones was to perform a CFD analysis of an entire high-lift aircraft from CAD to post-processed solution in 50 working days. This milestone was met with a simulation of a Boeing 777-200 landing configuration using an overset structured grid approach, and newly developed scripting software.[3] This accomplishment is a reduction by an order of magnitude in the CFD process time over what was possible three years earlier.

In addition to cycle time issues, a number of other challenges faced by the AST high-lift CFD team were put forth in a report.[4] These issues account for the fact that the current predictive accuracy of 3D Navier-Stokes methods for high-lift flows could not be readily assessed: there was a lack of sufficient 3D experimental high-lift data; only a limited number of 3D high-lift simulations had been conducted, and the available simulations had been done on relatively simple geometries; such simulations required significant computational and labor resources; and most viscous computational approaches were not able to simulate the complex geometries found on a high-lift aircraft configuration.

The success of the development of new overset CFD tools,[3] together with the computational and labor resources of the AST program, has removed many of these obstacles. The result is the ability to perform viscous CFD simulations for a number of complex high-lift configurations and compare them to experimental data, thus providing an accuracy assessment for Navier-Stokes applications to high-lift aircraft. In two companion papers, results are presented for the application of the overset CFD method to the flow over a High-Wing Transport aircraft with externally blown flaps,[5] and the flow over a three-element trapezoidal wing.[6] The current work presents new results for the computed flow over a over a Boeing 777-200 aircraft configured for landing. The current work attempts to validate the overset CFD approach for high-lift aircraft by comparing the computed results to experimental data obtained in the NASA Ames 12-Foot Pressure Wind Tunnel.

In the following sections, this paper presents the geometry and grids used in the current analysis, presents some initial results for the lift coefficient, shows the effects of sealing a spanwise gap between two leading-edge components and the effect of adding of a nacelle chine, and presents detailed pressure coefficient comparisons between computed and experimental data for several angles of attack.

Geometry and Grids

The computations simulate a 4.2%-scale, full-span model of the Boeing 777-200 aircraft as tested in the NASA Ames 12-Foot Pressure Wind Tunnel. A photograph of this model is shown in Fig. 1. The major aircraft components included in the computational and experimental models are the fuselage, the main wing, the inboard and outboard leading-edge slats, the Krueger slat, the inboard and outboard flaps, the flaperon, the flow-through engine nacelle and core-cowl, the engine strut, and the vertical tail. Although landing gear is shown in Fig. 1, the CFD results were compared with experimental runs with the landing-gear off. The experimental model also included a chine on the inboard side of the nacelle. Initially, CAD data for this component could not be found, and so was not included. The definition of the chine was obtained later and then added to the computational model, as described in a later section. Other details of the model include "steps" along the leading-edge of the main wing: the side-of-body (SOB) step, a step near the strut, and an outboard (OB) step near the wing tip. The surface grids for the SOB step and the OB step are shown in Figs. 2a and 2b, respectively.

Fig. 1. Boeing 777-200 wind-tunnel model.

In order to simplify the individual component grid generation, the seals between the flaps and flaperon are omitted. In the experiment, the flaps and flaperon are partially sealed together. This is done using wax and/or tape after the components are installed for each rigging. Thus, the CAD definition of the components do not represent the actual wind-tunnel model in this regard. As shown in Fig. 3, two small spanwise gaps (about 0.5% of the mean aerodynamic chord) are present between the flap elements in the computational model. It was anticipated that these small gaps would only have a minor effect on the flow solution. The inboard end of the inboard flap is partially sealed against the fuselage in the wind-tunnel model. In contrast, It was expected that this seal would have a non-negligible effect on the flow. Therefore, the sealing of the inboard flap against the fuselage was modeled in the computation.

At the leading edge, in the vicinity of the strut,

Fig. 4 shows a close-up of the surface grids on the wing leading edge, the Krueger slat, and the inboard slat. Small gaps exist at either end of the Krueger for the CFD model whereas for the wind tunnel model, the spanwise ends of the Krueger were partially sealed against the strut and inboard slat with wax and tape. These small gaps allow the grid generation for each component to proceed independent of the placement of neighboring components. The ends of the flap and slat elements are resolved using wingcap grids that in previous work[7] have been shown to adequately resolve the geometry and near-body flow-field.

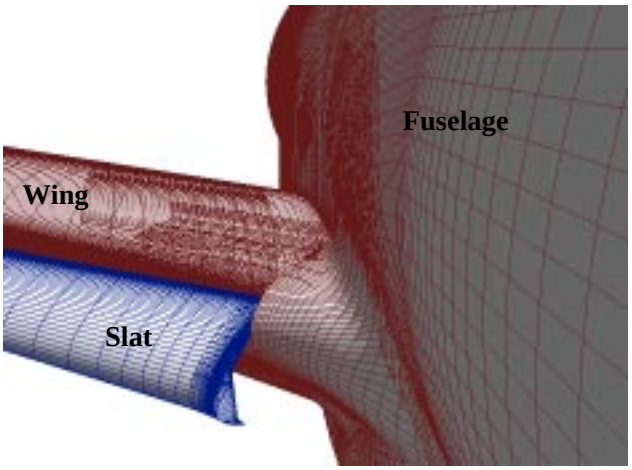

a. Side-of-body step.

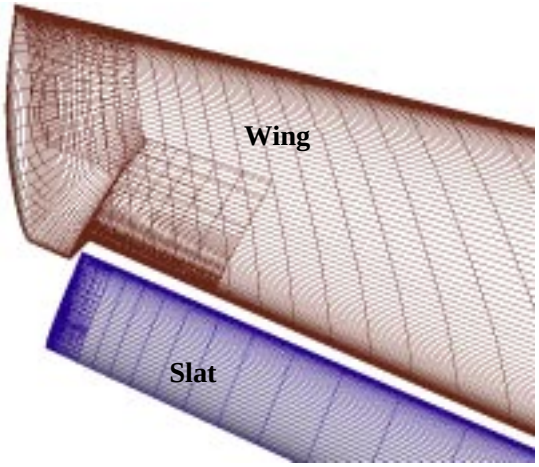

b. Outboard step.

Fig. 2. Spanwise steps in the wing leading edge.

Both the leading-edge and trailing-edge brackets are omitted from the CFD model. Trailing-edge flap-bracket fairings are expected to have a larger impact on the flow than the brackets, and so the three largest flap-bracket fairings are included in the computational simulation: the outboard fairing on the inboard flap and the inboard and outboard fairings on the outboard flap. A closer view of the inboard fairing is shown in Fig. 5. The fairings are positioned with and sealed against the underside of the wing, but are not connected to the flap surface.

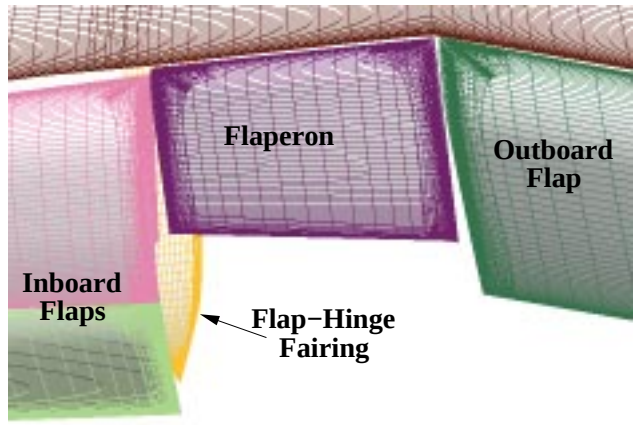

Fig. 3. Gaps between flaps and flaperon.

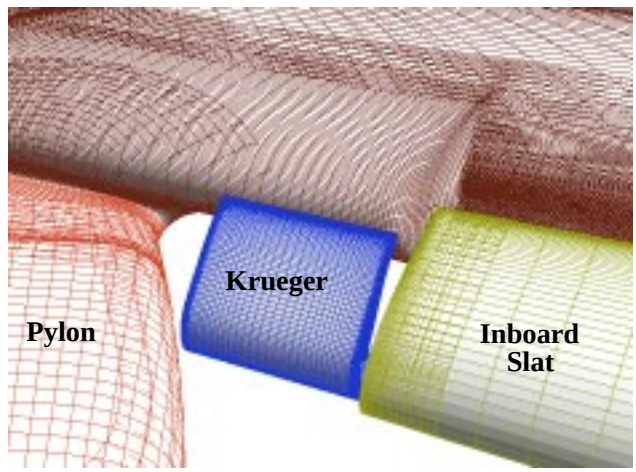

Fig. 4. Leading-edge spanwise gaps.

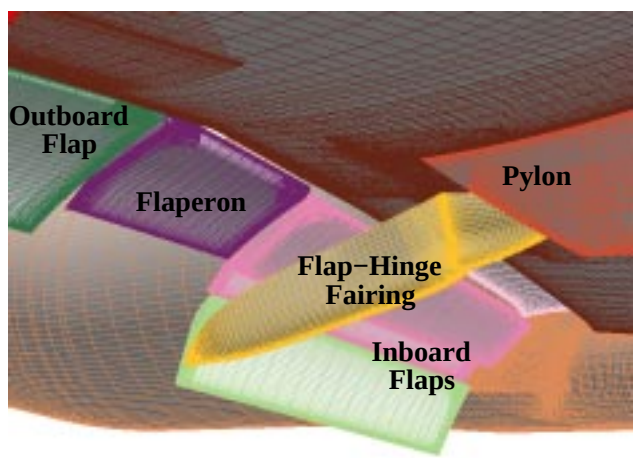

Fig. 5. Inboard flap-bracket fairing.

The entire grid-system for the Boeing 777-200 was generated on an SGI Octane workstation, with two R10000 195 MHz processors, 896MB of memory, and 13GB of disk space. The execution of the script system which runs the entire grid generation process from the original surface definition to the final grid system requires five hours on this machine. The resulting

grid system for the Boeing 777-200 aircraft configured for landing consists of 22.4 million grid points within 79 overset zones. A view of the surface grids on the entire configuration is shown in Fig. 6, which plots only every fourth grid line in each computational direction for clarity. An attempt was made to generate grids that would be adequate for all expected flow features based on previous high-lift CFD problems, most of which were simulations of two-dimensional multi-element airfoils. Grid spacing of 10^{-6} times the mean aerodynamic chord is applied normal to the surface. This results in y^+ values on the order of 1.0 for the first grid point off the surface. Also, the maximum grid-stretching ratio in the normal direction is limited to 1.25. A total of 5617 orphan points (approximately 0.02% of the total points) remained within the grid system after the overset process; averaging is used to update these points within the flow solver. An orphan point is a boundary point requiring interpolated solution data from a neighboring grid, but for which the software cannot find a neighbor grid with adequate overlap.

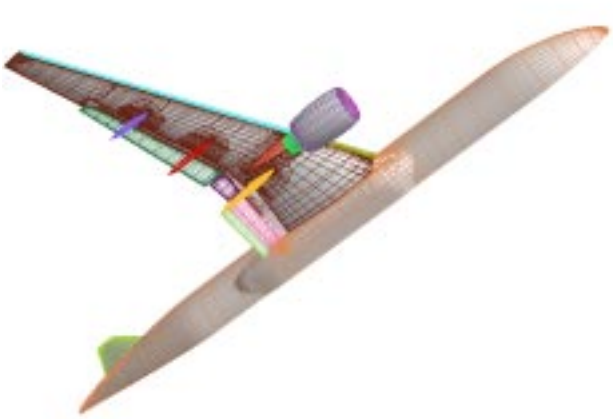

Fig. 6. Surface grids on Boeing 777-200.

B777 Flow Simulation and Analysis

Flow Solver

The OVERFLOW[8,9] Navier-Stokes flow solver was used in all of the current computations. This code is written to be efficient for computing very large-scale CFD problems on a wide range of supercomputer architectures. On vector supercomputers with very fast secondary memory devices, the OVERFLOW code includes an out-of-core memory management option, such that the total memory used is a function of the largest zone in the grid system, not the total number of grid points. The code is efficiently vectorized, and is written to execute simultaneously on multiple shared-memory processors. For cache-based multiple-processor machines, the code has been parallelized using both a shared memory algorithm, and with a Message-Passing Interface (MPI) library for non-shared memory systems. For more details, see the works by Jespersen[10] and Taft.[11] Approximately half of the current cases were run using the standard OVERFLOW, version 1.8b, while the rest of the cases were run using OVERFLOW-MLP version 1.8k. The former cases were run on a 16 processor Cray C90 computer, and the MLP version was run on an SGI ORIGIN 2000 machine with 256 processors.

All of the current OVERFLOW computations utilized the third-order Roe upwind-differencing[12] option, and the Spalart-Allmaras turbulence model[13] with the flow assumed to be fully-turbulent. In the experimental investigation of the 777, no boundary-layer trips were used, and there was no measurement of transition locations. The prediction and modeling of transition for complex 3D geometries is beyond the capability of the OVERFLOW code. The viscous terms in all three directions are computed, however the cross-derivative viscous terms were not included. These were not used because they add about 10% to the cost of the computation, and because previous test cases have shown that their use does not affect the solution. The multi-grid option[9] to the code was used with three levels. Each OVERFLOW case is run using a local time-step scale of 0.1, a minimum CFL number cutoff for the locally varying time-stepping (CFLMIN) of 5.0, and a CFL number multiplier for the turbulence model (CFLT) of 4.0. Low Mach number pre-conditioning is not used because this option caused the code to become unstable for the 777 grid system. In these computations, the code was considered converged to a steady-state when the L2 norm of the right-hand side had dropped at least 2 or 3 orders of magnitude for each computational grid, and when the variation in the total lift coefficient was less than 0.01% over the last 100 cycles.

Flow Conditions

The simulation conditions for the current analysis corresponded to data acquired during wind tunnel Run 421 in the NASA Ames 12-Foot Pressure Wind Tunnel. The model was configured for landing as defined by the Flaps-30 setting. The flow had a free-stream Mach number of 0.2, a total pressure of 4.5 atmospheres and a Reynolds number based on the mean aerodynamic chord of 5.8 million. The simulation was conducted in free-air; no wind-tunnel mounting hardware was modeled. The experimental data used for the comparisons was corrected for wind-tunnel wall and blockage interference, but excludes tare and interference corrections for the bi-pod mounting device.

Five solutions were computed using the grid system for the initial geometry. These were computed at angles of attack (α) of 4, 8, 12, 16, and 20 degrees. The

cases at $\alpha = 4$ and 8 degrees were restarted from solutions obtained on an initial grid system that did not include the flap-bracket fairings. Such restarts save only a small percentage of the computing time compared to the free-stream initial conditions, even though the change from the restarted solution is small. As a point of reference, the difference in CL at $\alpha = 8$ degrees with the addition of the flap fairings was 1.8% lower, and the drag coefficient (CD) was 1.5% lower. Figure 7 shows the convergence history for CL for the cases computed at 4, 8, and 12 degrees angle of attack. Due to the proprietary nature of this data, the values cannot be included on the y-axis of this and other subsequent plots. These three cases converged in an average of 2160 cycles, and required an average of 194 C90 CPU hours per case. This convergence rate is fairly typical of all runs, however the cases at higher angles of attack usually require more cycles.

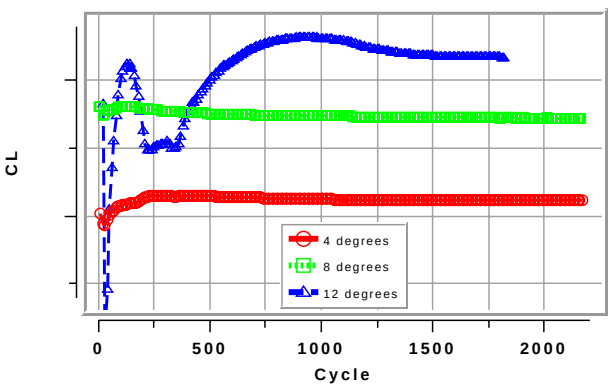

Fig. 7. Convergence of lift coefficient.

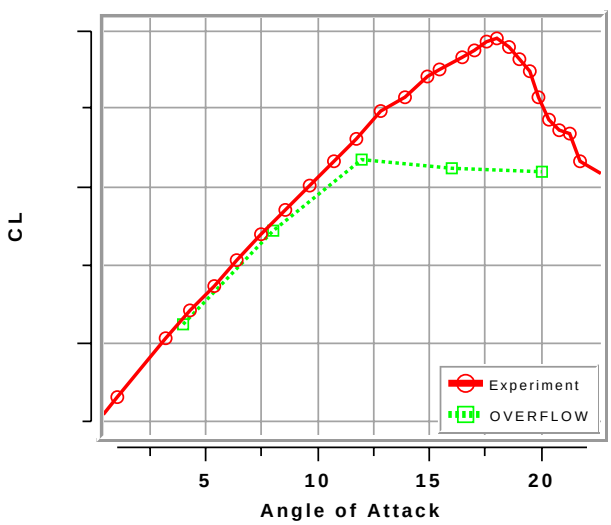

Fig. 8. Lift coefficient versus angle of attack.

The lift polars for the first five runs are plotted in Fig. 8. The computed CL differs from the experimental lift by less than 2 percent for the lower angles of attack. However, this figure shows that the computed flow stalls at a much lower angle of attack than the experiment. Further investigation of the solution at $\alpha = 16$ degrees shows that the Krueger slat experiences separated flow.

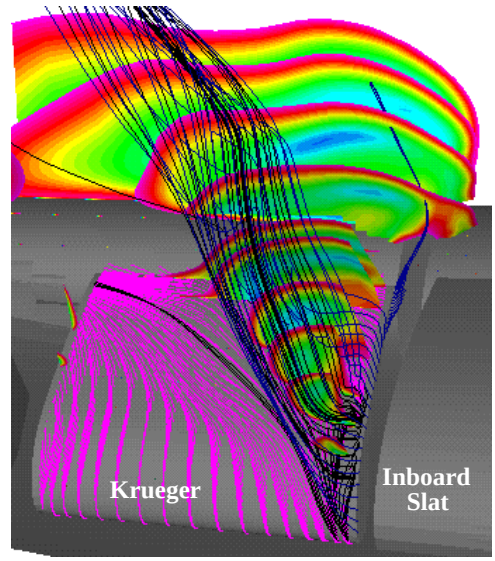

a. Close view of flow over Krueger.

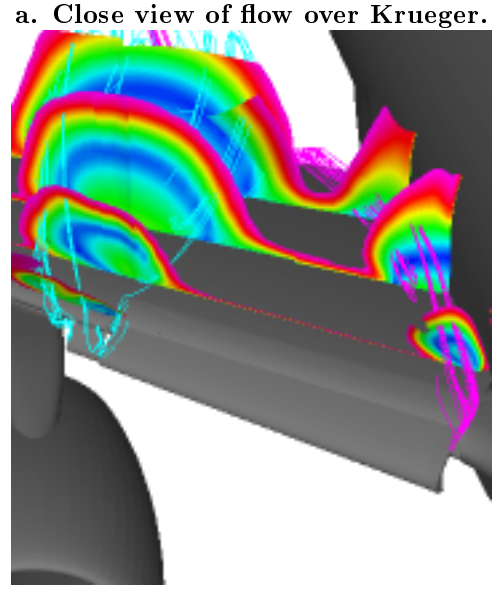

b. View of inboard portion of wing.

Fig. 9. Mach contours and particle traces at $\alpha = 16$ for initial geometry.

Figure 9 shows a close-up of the flow over the Krueger using both particle traces and Mach-number contours. The solid Mach-number contours are drawn in the range of 0.0 to 0.1, and show regions of slower flow. This figure shows how a vortex is formed by flow traveling upward through the small gap between the Krueger and the inboard slat. This vortex flows over the top of the Krueger, lifting the flow off the surface of the Krueger, causing the flow to separate. In Fig. 9b, it can be seen that as this passes onto the upper surface of the wing, the adverse pressure gradient causes rapid expansion, creating a large stall region on top of the wing.

These results suggest that one source of the discrepancy between the computations and the experiment at high angles of attack is the small spanwise gap in the computational model between the Krueger slat and the inboard slat. In the experiment, this gap is partially sealed using tape and wax; the exact experimental geometry is difficult to duplicate. In an effort to seal this gap, the two elements were combined into a single inboard slat element, which creates the maximum amount of sealing possible. This modification required a slight rounding of the wing leading edge step. Figure 10 shows an image of the modified Krueger and inboard slat.

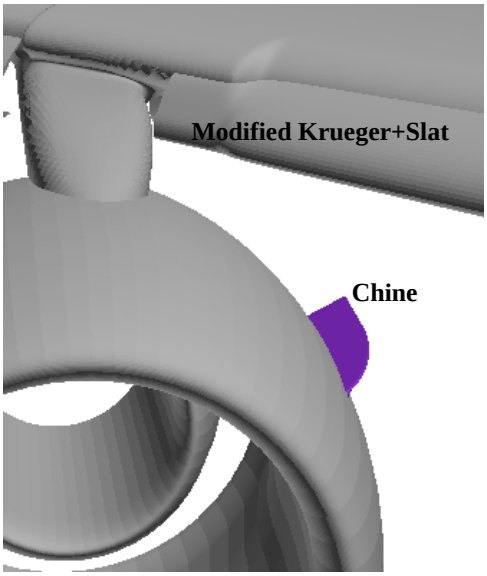

Fig. 10. Modified Krueger and inboard slat, and the chine mounted on the nacelle.

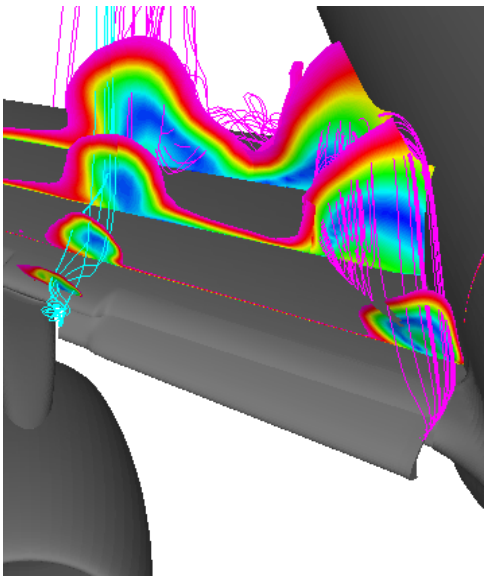

Fig. 11. Mach contours and particle traces at $\alpha = 16$ for sealed Krueger and slat.

A second grid system was built with this geometry modification and a flow case was run at an angle of attack of 16 degrees. The lift coefficient for this new run was only about 3% higher than the previous case, and so the result was not as dramatic as expected. At the time this case was run, a CAD representation of the nacelle chine was finally located, and so this piece of the geometry was added to the computational model. Figure 10 shows the chine mounted on the inboard side of the nacelle. A third grid system was built with the chine added to the second grid system, and another case was run at an angle of attack of 16 degrees. This resulted in a CL which was about 5% higher than the first grid system calculation at this angle of attack, which is still significantly lower than the experimental lift. A single grid was used to add the chine, which provided resolution for the near wake of the chine, but did not provide extra resolution for the vortex as it convects downstream over the wing. While the wing grid has adequate off-body resolution for the slat wake, the chine vortex may not have adequate grid resolution.

Figures 11 and 12 show plots of Mach-number contours and particle traces over the inboard region of the wing for these two geometry modifications. Figure 11 includes just the sealing of the Krueger and slat spanwise gap, and Fig. 12 shows the flow after addition of the chine to this geometry. The sealing of the slats does reduce the amount of low-speed flow over the wing aft of the strut, however it also increases the amount of separated flow at the wing root. The addition of the chine further reduces the amount of low-speed air aft of the strut and nacelle.

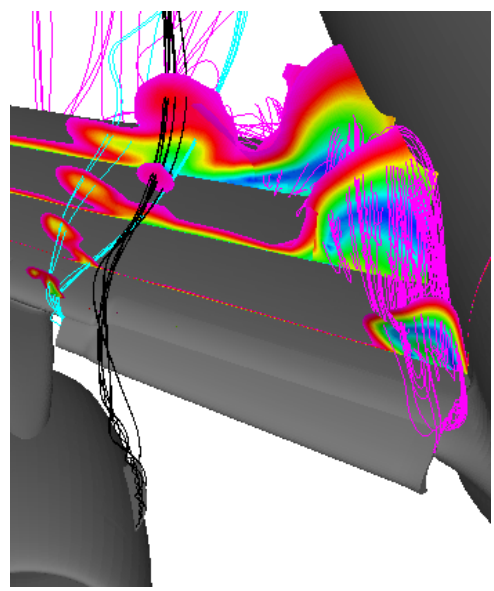

Fig. 12. Mach number and particle traces at $\alpha = 16$ with addition of chine.

The third geometry with the sealed slats and the chine was also used to compute the flow at angles of attack of -5.5, -1.1, 4, 8, 12, and 20 degrees. The lift coefficient versus angle of attack is plotted in Fig. 13

for this geometry, together with the experimental results and the results from the first geometry. Figure 14 plots CD versus α. The results from the third geometry show even better agreement with experimental lift for the lower angles of attack; at $\alpha = 4$, 8, and 12, the differences in lift are all less than 1.5%, and the differences in drag average 4%.

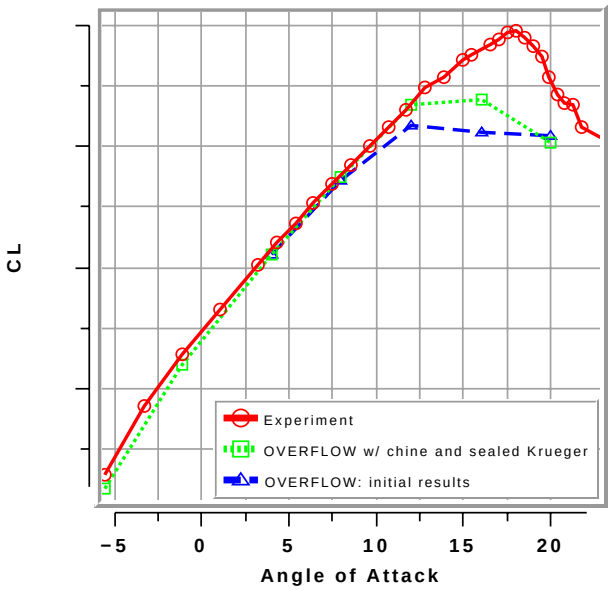

Fig. 13. Lift coefficient versus α

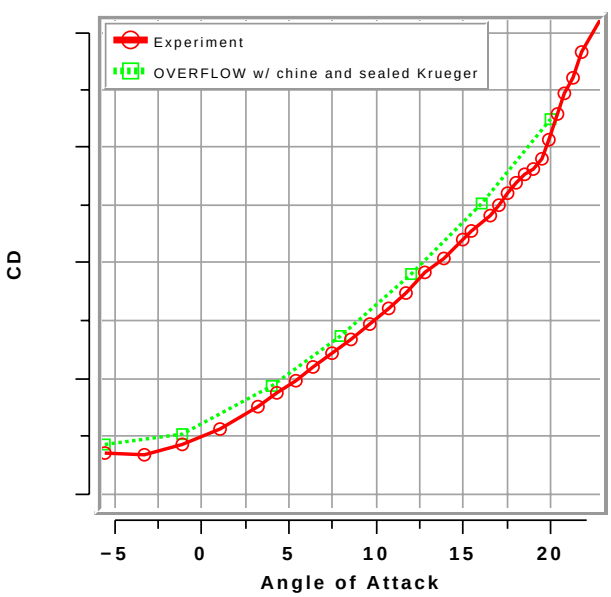

Fig. 14. Drag coefficient versus α

Pressure Coefficient Results

The pressure coefficient (Cp) data is presented here for the third geometry. The Cp data is plotted for spanwise locations of 13%, 20%, 30%, 60%, and 79%; these locations are illustrated in Fig. 15.

In the next six figures, Cp is plotted versus the scaled chord-wise coordinate, x/c, where c is the local chord for the particular element. The x-axes are scaled differently for the slat, wing, and flaps so that data for the smaller elements can be seen. The first column in the plot is the slat, the second is the main wing, and the remaining columns are the flaps. The CFD results are plotted with solid lines, and the experimental results are plotted with circles. Within each individual figure, the Cp scale is the same for all of the spanwise cuts. The computational results are compared with experimental data from the nearest corrected angle of attack available. The reason that many of the cases were computed at angles of attack not corresponding to a corrected experimental α is that none of the experimental data was made available to the high-lift CFD team until after several cases were initially computed. Note that the only experimental data available for the leading-edge devices is on the Krueger at the 30% span station.

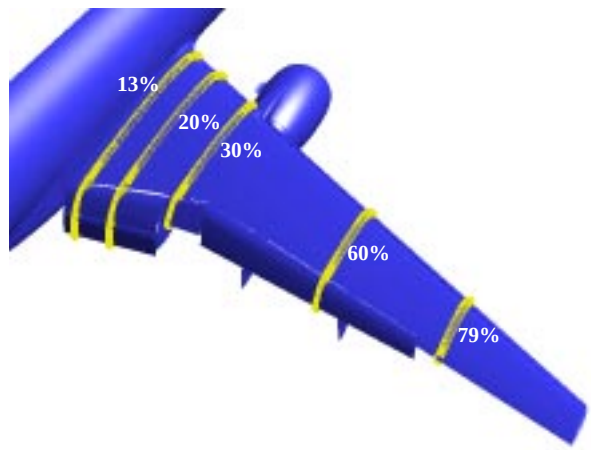

Fig. 15. Spanwise locations of the Cp data.

The Cp data is plotted in Figs. 16–21 for angles of attack of -5.5, 4, 8, 12, 16, and 20 degrees angle of attack. In general, good agreement is seen between the experiment and the computations. One region in which there is consistently a difference is on the inboard end of the leading inboard flap, on the upper-surface. Here, the computed suction peak is consistently higher than the experimental results, producing more lift in the computations on the leading inboard flap and the main wing than in the experiment. This location is very close to the rear bi-pod support in the experimental model, which includes a very large hole on the underside of the fuselage near this flap. This is a possible cause for this discrepancy. Other than this difference, the agreement between the experiment and computation for $\alpha = 4$, 8, and 12 is excellent. In particular, the indication of flow separation on the outboard flap is seen at 60% span in both the experiment and the computation by a flat section in the pressure curve over the aft portion of the upper surface at these angles of attack.

Figure 20 shows the results at 16 degrees angle of attack. The inboard Cp data shows a picture consistent with Fig. 12: the computed flow is stalled at the wing root. The experimental Cp data shows a much higher leading-edge suction peak, indicating that it has not stalled at the wing root.

Figure 21 shows Cp data at 20 degrees angle of attack. This shows that in both the experiment and the computed flow, the wing is stalled at all the inboard sections, but still attached at the outboard sections. The computed upper surface pressures are consistently higher than the experiment, and thus the computed lift is too low.

The reason for this large discrepancy at higher angles of attack is not known at this time. Possible reasons for the early stalling of the CFD model include: a discrepancy between the computational and experimental geometries; inadequacies in the turbulence modeling; transition effects; insufficient grid resolution in the wing-root region or at the inboard end of the inboard slat; and wind-tunnel effects, including both wind-tunnel walls and bi-pod mounting effects. The possibility of a difference in the geometry is an issue, even though it is believed that the computational model of the inboard slat is trimmed at the same inboard plane as the experimental model, a small difference in the spanwise extent of this element can greatly effect the flow over the wing root. Given additional time and resources, the first thing to try would be to extend the inboard slat spanwise so that it seals against the fuselage, which should maximize the lift generated by the inboard wing.

Summary and Conclusions

An overset approach has been used to compute the flow over an entire Boeing 777-200 aircraft configured for landing. The computed results have been compared with experimental data acquired in the NASA Ames 12-Foot Pressure Wind Tunnel. Good agreement between the two is seen for the lift and drag coefficients at lower angles of attack: at approach conditions, the computational lift is within 1.5% of the experiment, and the computed drag is within 4%. However, the computational model under-predicts the lift at higher angles of attack, and misses maximum lift by nearly 11%. Several differences between the experimental model and the computational geometry exist. Most of these differences involve spanwise gaps between high-lift elements which are not present in the wind-tunnel model. The effect of completely sealing the gap between the inboard slat and the Krueger slat was demonstrated, as was the effect of adding the inboard chine. Both had a dramatic effect on the flow over the wing aft of the strut and nacelle, but did not dramatically increase the lift as the flow over the wing root began to stall.

The current work represents a big improvement in the ability to perform viscous CFD analysis of high-lift aircraft. The use of the overset-grid approach makes it possible to develop a grid system for a complete high-lift aircraft in several working weeks, which can then be used to study design trades-offs with only a few days of work. The computational cost of computing numerous conditions, however, is substantial. The accuracy of the current approach is excellent at lower angles of attack, but the inability to compute maximum lift will limit the usefulness of viscous CFD analysis as a production design tool. Further work needs to be done to understand the reason for the poor agreement at maximum-lift conditions.

Acknowledgments

The authors would like to acknowledge the technical help of Dr. Pieter Buning, NASA Langley Research Center, as well as the AST/IWD program management for their dedication and insight. They also wish to acknowledge the helpful comments from Dr. Thomas Coakley and Dr. Scott Lawrence in their review of this work. This work was partially funded by the Advanced Subsonic Technology Program through NASA contract NAS2-20268.

References

[1] Lynch, F. T., Potter, R. C., and Spaid, F. W., "Requirements for Effective High Lift CFD," ICAS Proceedings, 20th Congress, Sept. 1996.

[2] Meredith, P. T., "Viscous Phenomena Affecting High-Lift Systems and Suggestions for Future CFD Development," *High-Lift System Aerodynamics*, AGARD CP-515, Paper No. 19, Sept. 1993.

[3] Rogers, S. E., Roth, K., Nash, S. M., Baker, M. D., Slotnick, J. P., Cao, H. V., and Whitlock, M., " Advances in Overset CFD Processes Applied to Subsonic High-Lift Aircraft," AIAA Paper 2000-4216, Aug. 2000.

[4] Bussoletti, J., Johnson, P., Jones, K., Roth, K., Slotnick, J. P., Ying, S., and Rogers, S. E., "The Role of Applied CFD within the AST/IWD Program High-Lift Subelement: Applications and Requirements," AST/IWD Program Report, June 1996. To be published as a NASA TM.

[5] Slotnick, J. P., An, M. Y., Mysko, S. J., Yeh, D. T., Rogers, S. E., Roth, K., Baker, M. D., and Nash, S. M., "Navier-Stokes Analysis of a High-Wing Transport High-Lift Configuration with Externally Blown Flaps," AIAA Paper 2000-4219, Aug. 2000.

[6] Rogers, S. E. and Nash, S. M., "CFD Validation of High-Lift Flows With Significant Wind-Tunnel Effects," AIAA Paper 2000-4218, Aug. 2000.

[7] Rogers, S. E., Cao, H. V. and Su, T. Y., "Grid Generation For Complex High-Lift Configurations," AIAA Paper 98-3011, June 1998.

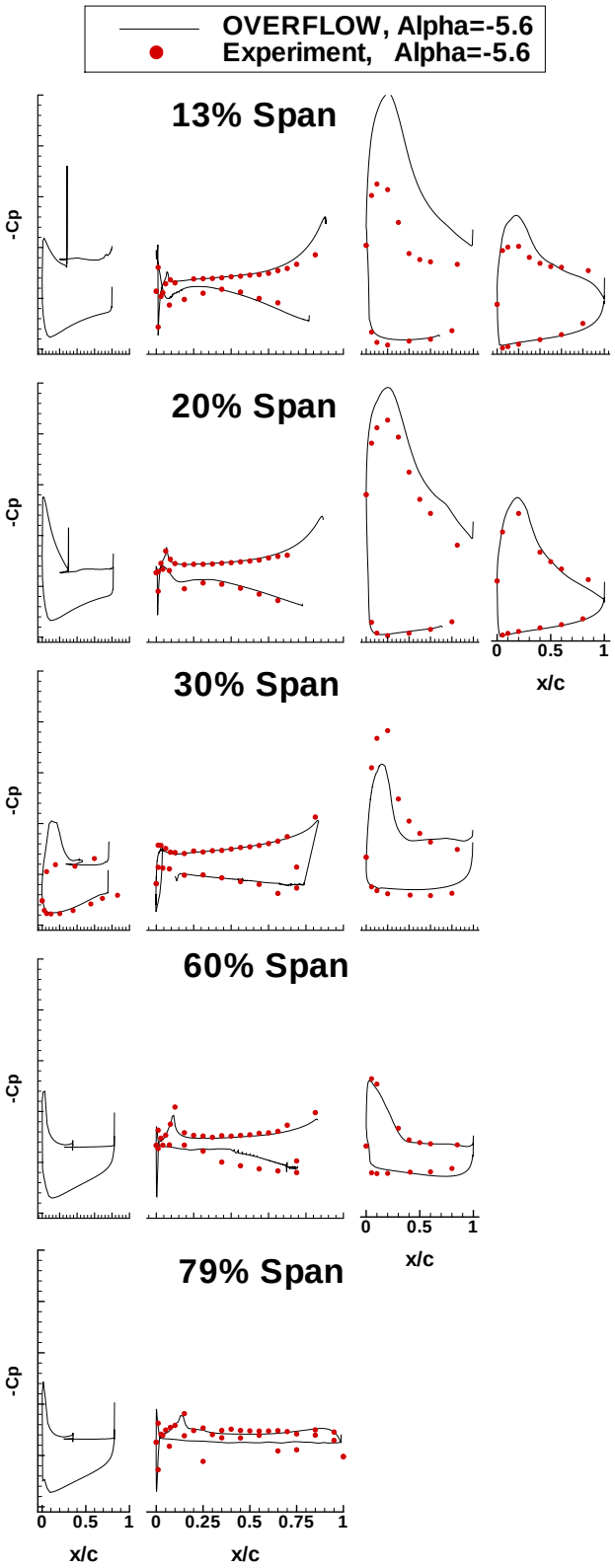

Fig. 16. Cp data for α = -5.6 deg.

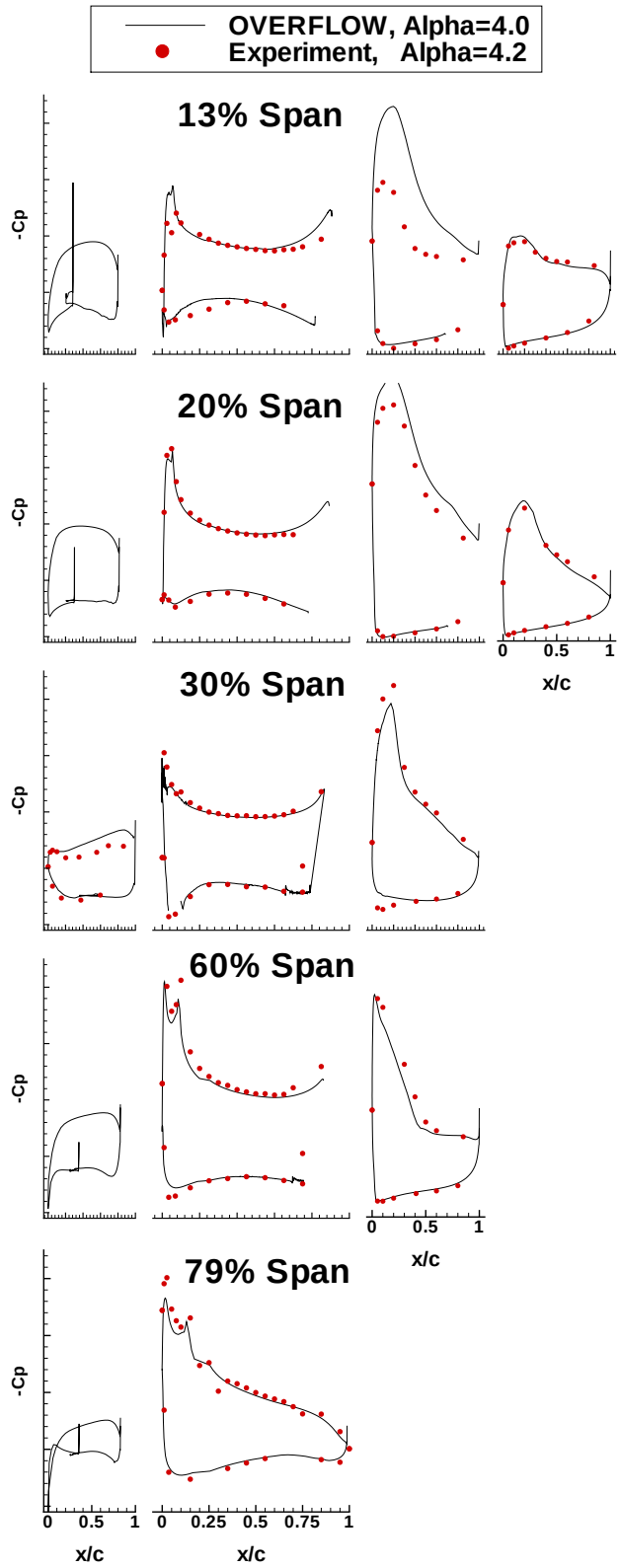

Fig. 17. Cp data for α = 4 deg.

[8] Buning, P. G., Jespersen, D. C., Pulliam, T. H., Chan, W. M., Slotnick, J. P., Krist, S. E., Renze, K. J., "OVERFLOW User's Manual, Version 1.8b," NASA Langley Research Center, Hampton VA, 1998.

[9] Jespersen, D. C., Pulliam, T. H., and Buning, P. G., "Recent Enhancements to OVERFLOW," AIAA Paper 97-0644, Jan. 1997.

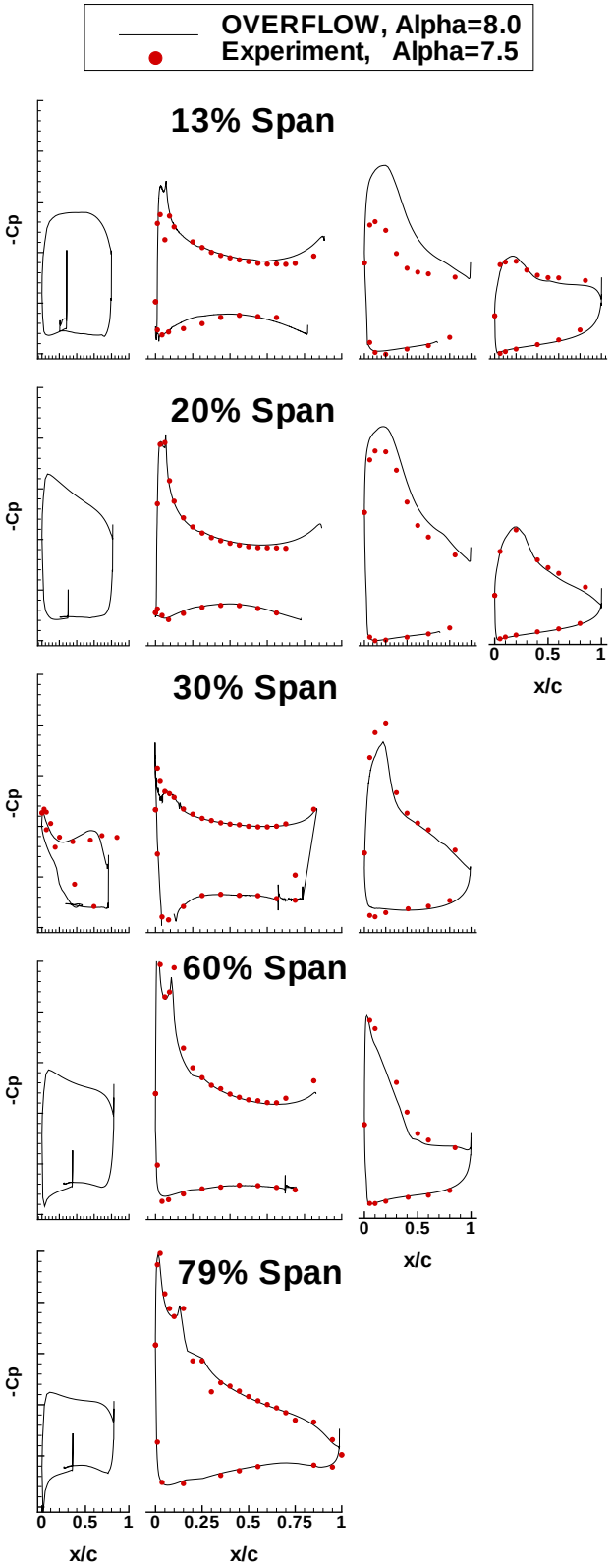

Fig. 18. Cp data for $\alpha = 8$ deg.

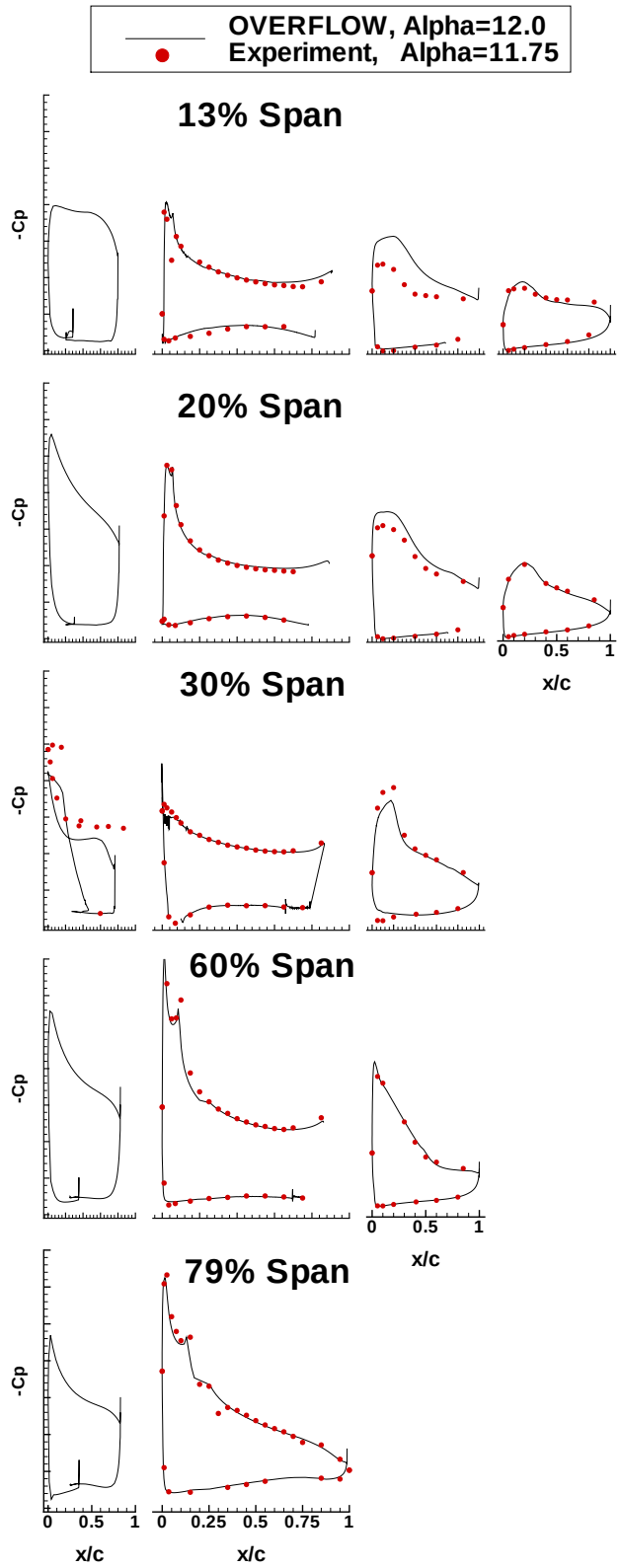

Fig. 19. Cp data for $\alpha = 12$ deg.

[10] Jespersen, D. C., "Parallelism and OVERFLOW," NAS Technical Report NAS-98-013, October 1998. http://www.nas.nasa.gov/Pubs/TechReports/NASreports/NAS-98-013/

[11] Taft, J., "OVERFLOW Gets Excellent Results on SGI Origin2000," *NAS News*, Vol. 3, No. 1, Jan. 1998. http://www.nas.nasa.gov/Pubs/NASnews/98/01/overflow.html

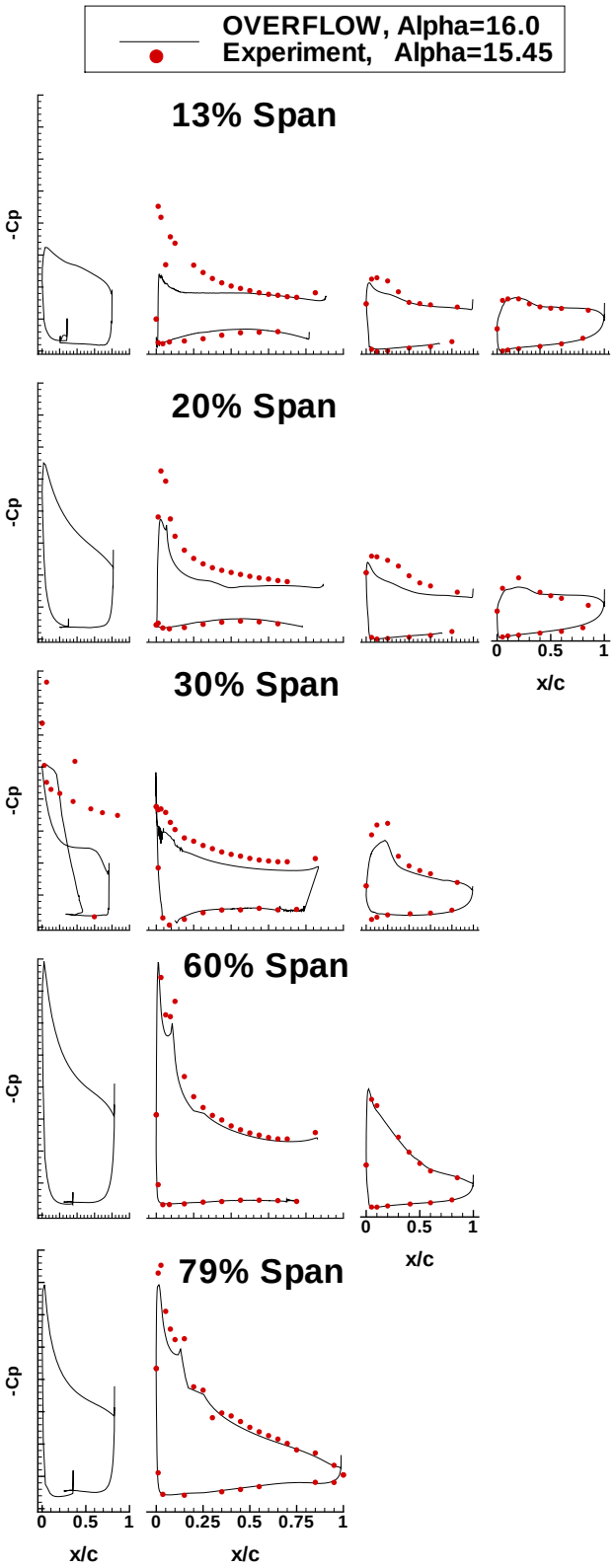

Fig. 20. Cp data for $\alpha = 16$ deg.

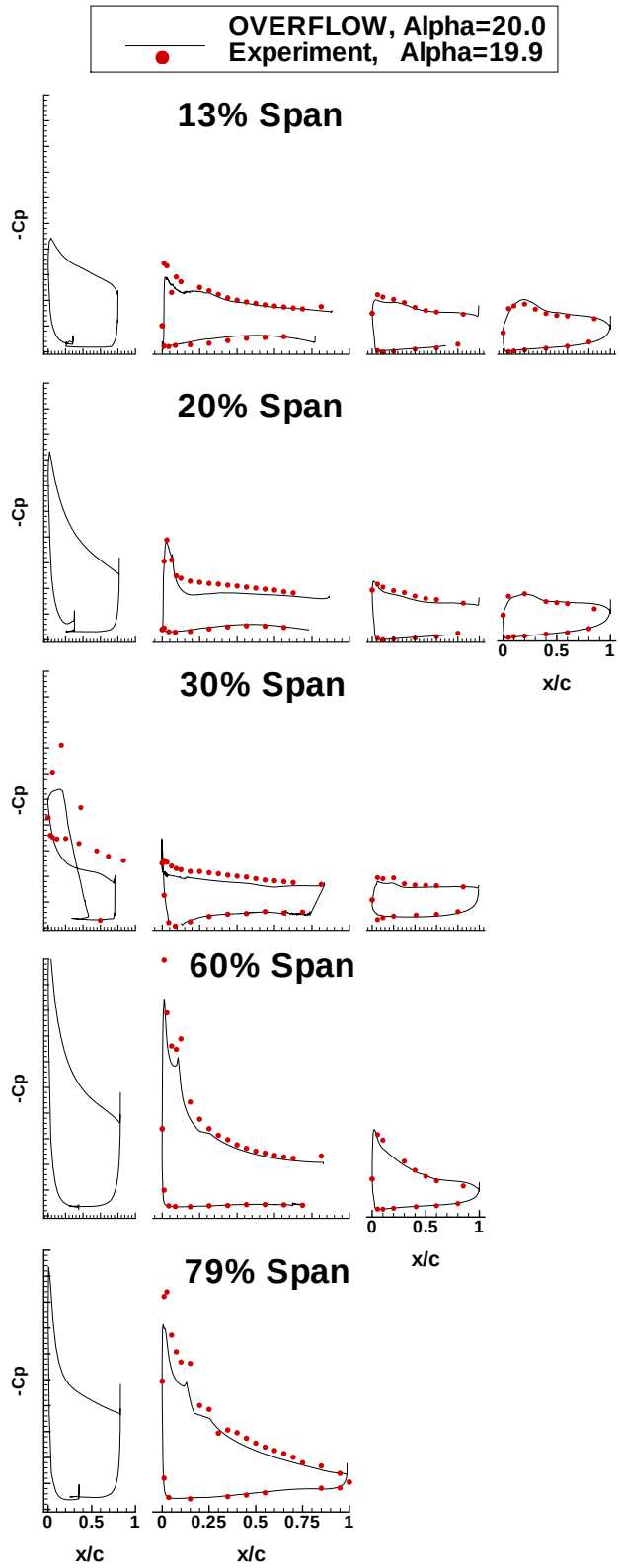

Fig. 21. Cp data for $\alpha = 20$ deg.

[12] Roe, P. L., "Approximate Riemann Solvers, Parameter Vectors, and Difference Schemes," *J. Comput. Phys.*, Vol. 43, pp. 357–372, 1981.

[13] Spalart, P. R. and Allmaras, S. R., "A One-Equation Turbulence Model for Aerodynamic Flows," AIAA Paper 92-0439, Jan. 1992.